Ceramics International 43 (2017) 12979–12982

Contents lists available at ScienceDirect

Ceramics International

journal homepage: www.elsevier.com/locate/ceramint

Short communication

Enhanced fracture toughness of Al and Bi co-doped Mg_2Si by metal nanoparticle decoration

Gwansik Kim[a], Hwijong Lee[a], Jeongmin Kim[a], Jong Wook Roh[a], Inwoong Lyo[b], Byung-Wook Kim[b], Kyu Hyoung Lee[c,*], Wooyoung Lee[a,*]

[a] Department of Materials Science and Engineering, Yonsei University, Seoul 03722, Korea
[b] Advanced Materials Research Team, Central Advanced Research and Engineering Institute, Hyundai Motor Company, Uiwang 16082, Korea
[c] Department of Nano Applied Engineering, Kangwon National University, Chuncheon 24341, Korea

ARTICLE INFO

Keywords:
Nanoinclusion
Thermoelectric
Mg_2Si
Nanometal decoration
Fracture toughness

ABSTRACT

We herein report the effects of metal nanoinclusions (Cu, Al, and Sn) embedded at grain boundaries on the thermoelectric transport and mechanical properties of Mg_2Si-based compounds. Hybrid powders of microscale Al and Bi co-doped Mg_2Si ($Mg_{1.96}Al_{0.04}Si_{0.97}Bi_{0.03}$) and nanoscale metal particles were synthesized by a nanometal decoration technique and their nanocomposites were fabricated by a spark plasma sintering process. In compacted polycrystalline bulks, homogeneous dispersion of metal nanoparticles (~150 nm) was readily achieved at grain boundaries. The thermoelectric performance of the nanocomposites deteriorated mainly because of the reduced mobility owing to intensified electron scattering at the phase boundaries between the Mg_2Si matrix and metal nanoinclusions, while the fracture toughness (~1.10 MPa $m^{1/2}$, 35% improvement) was significantly enhanced on introducing Al nanoparticles.

1. Introduction

Thermoelectric (TE) power generation is one of the most promising energy conversion technologies from waste heat in various industrial fields. Recently, automotive TE generators (ATEGs) have received significant attention as they facilitate the improvement of the fuel efficiency of a vehicle. For the wider applications of TE power generation (TEG) devices, the development of high-performance and low-cost bulk-type TE materials is necessary. Mg_2Si-based compounds are good candidates, especially for ATEGs, because of their abundance, nontoxicity, and low density (~1.99 g cm^{-3}) compared to that of other mid-to-high-temperature TE materials such as filled skutterudites and half-Heusler alloys. In previous studies, we developed high-TE-performance Mg_2Si-based compounds by adopting a doping approach, as evaluated by the dimensionless figure of merit ZT (= $\sigma S^2T/\kappa_{tot}$, where σ, S, T, and κ_{tot} are the electrical conductivity, Seebeck coefficient, absolute temperature, and total thermal conductivity, respectively). A peak ZT value of ~1.02 was obtained at 873 K for the polycrystalline bulk of Al and Bi co-doped Mg_2Si, fabricated by the combined technique of a two-step solid-state reaction and spark plasma sintering (SPS) [1]. Very recently, we evaluated the feasibility of our synthetic process for commercial-scale production, and obtained good reproducibility as well as a moderate ZT of 0.82 at 873 K for a 1-kg batch-scale sample we prepared [2].

Superior mechanical property is another essential prerequisite since the temperature difference between the hot and cold sides of the TEG module would lead to severe thermal and mechanical stress under operating conditions. Moreover, Mg_2Si-based compounds can easily undergo fracture owing to their inherent brittle fracture characteristics [3,4]. It is important to prevent or deflect propagating cracks induced by stress by improving the fracture toughness. One common strategy for enhanced fracture toughness involves the use of nontraditional processing technologies such as pressure-induced sintering; however, its effect is limited to the intrinsic property of the materials [5,6]. Another approach for improved fracture toughness of TE materials is the introduction of nanophases with high fracture toughness, such as PSZ (partially stabilized ZrO_2), Al_2O_3, SiC, CNTs (carbon nanotubes), or graphene [7–11]. However, enhanced mechanical properties are inevitably accompanied by a power factor (σS^2) reduction, mainly owing to intensified carrier scattering because of the inhomogeneous distribution and agglomeration of nanophases. Thus, a novel approach for the introduction of nanoparticles with reduced size and uniform distribution in the TE matrix is required to realize simultaneous enhancement of the TE and mechanical properties.

In the present study, we investigate the effects of metal nanoinclusions (Cu, Al, and Sn) on the TE transport parameters and fracture toughness of Mg_2Si-based compounds in an effort to obtain high TE

* Corresponding authors.
E-mail addresses: khlee2014@kangwon.ac.kr (K.H. Lee), wooyoung@yonsei.ac.kr (W. Lee).

http://dx.doi.org/10.1016/j.ceramint.2017.06.002
Received 20 March 2017; Received in revised form 23 May 2017; Accepted 2 June 2017
Available online 03 June 2017

performance as well as enhanced mechanical properties. Using a nanometal decoration technique, we demonstrate the synthesis of hybrid powders of doped Mg_2Si and metal nanoparticles and that the metal nanoparticles were about 100–200 nm in size in the final bulk nanocomposites [12–14]. The *ZT* values of the nanocomposites were decreased on introduction of Cu, Al, and Sn nanoparticles mainly because of the reduced power factor, whereas a significantly enhanced fracture toughness ~1.10 MPa $m^{1/2}$ was obtained when the Al nanoparticles were introduced.

2. Experiment

Al and Bi co-doped Mg_2Si ($Mg_{1.96}Al_{0.04}Si_{0.97}Bi_{0.03}$) powders were synthesized by an up-scaled solid-state reaction detailed in our previous report [2]. The hybrid powders of $Mg_{1.96}Al_{0.04}Si_{0.97}Bi_{0.03}$ and metal nanoparticles were prepared by a mix-and-heat process. Metal acetates (copper(II) acetate, $(CH_3COO)_2Cu$; aluminum acetate, $(CH_3COO)_2(OH)Al$; tin acetate, $(CH_3COO)_2Sn$) and $Mg_{1.96}Al_{0.04}Si_{0.97}Bi_{0.03}$ powders were mixed using a high-energy ball mill (8000D, SPEX, USA) for 5 min. Then, the mixed powders were placed in a quartz boat and heated to remove the acetate (-CH_3COO-). Considering the melting points, the Cu- and Al-containing mixtures were heated at 300 °C for 2 h and the Sn-containing mixture was heated at 200 °C for 3 h in a mixed gas atmosphere (Ar 95% and H_2 5%).

The disc-shape compacted bulks were fabricated using SPS at 1023 K for 5 min under 70 MPa. The relative densities of all samples were 97–99% of the theoretical density. Phase analysis for the spark plasma sintered bulks was performed by X-ray diffraction (XRD, Ultima IV/ME 200DX, Rigaku, Japan) with CuKα radiation. The electronic transport properties (σ and S) from 300 to 873 K were measured by a TE measuring instrument (ZEM-3, ULVAC, Japan). The carrier concentration (n_c) and carrier mobility (μ_{Hall}) values at 300 K were obtained by Hall effect measurements under a 1 T magnetic field in the van der Pauw configuration. The κ_{tot} ($\kappa_{tot} = \rho_s C_p \lambda$) values were calculated from measurements taken separately. The λ values were measured under vacuum using the laser flash method (Netszch LFA-457, Germany) and the heat capacity (C_p) values were obtained using differential scanning calorimetry (DSC, DSC 8000, Perkin Elmer, USA). The microstructure of the spark plasma sintered bulks was analyzed by scanning electron microscopy (SEM, JEOL-7800F, JEOL Ltd., Japan).

The fracture toughness (K_{Ic}) was estimated by the following equation:

$$K_{Ic} = \chi\left(\frac{E}{H}\right)^{1/2}\frac{P}{a^{3/2}}$$

where P is the applied load, E is the Young's modulus, H is the Vickers hardness, a is the radial crack length measured from the center of the indent, and χ is a calibration constant taken to be 0.016 ± 0.004 [15]. The Vickers hardness and radial crack length was measured by a Vickers hardness tester (Mitutoyo_HM-101, Mitutoyo, Japan), with a load of 2.942 N and dwell time of 10 s.

3. Results and discussion

Fig. 1(a) shows the SEM image for the hybrid powders of $Mg_{1.96}Al_{0.04}Si_{0.97}Bi_{0.03}$ and $(CH_3COO)_2Cu$ after heat treatment at 300 °C. Thermal decomposition of nanoscale $(CH_3COO)_2Cu$ in a reducing atmosphere yielded Cu nanoparticles with an average size of ~150 nm; the Cu nanoparticles were attached to the $Mg_{1.96}Al_{0.04}Si_{0.97}Bi_{0.03}$ powder surface without severe aggregation. However, each hybrid powder had dense distributions of nanoparticles on its surface. These characteristic features were also observed for Al- and Sn-nanoparticle-decorated $Mg_{1.96}Al_{0.04}Si_{0.97}Bi_{0.03}$ powders. SEM images for the fractured surface of the spark plasma sintered nanocomposite fabricated from 0.6 vol% metal (Cu, Al, and Sn)-decorated $Mg_{1.96}Al_{0.04}Si_{0.97}Bi_{0.03}$ powders are shown in Fig. 1(b)–(d). Metal (Cu, Al, and Sn) nanoinclusions embedded at grain boundaries were clearly observed and their size remained at ~150 nm. The nanoinclusions

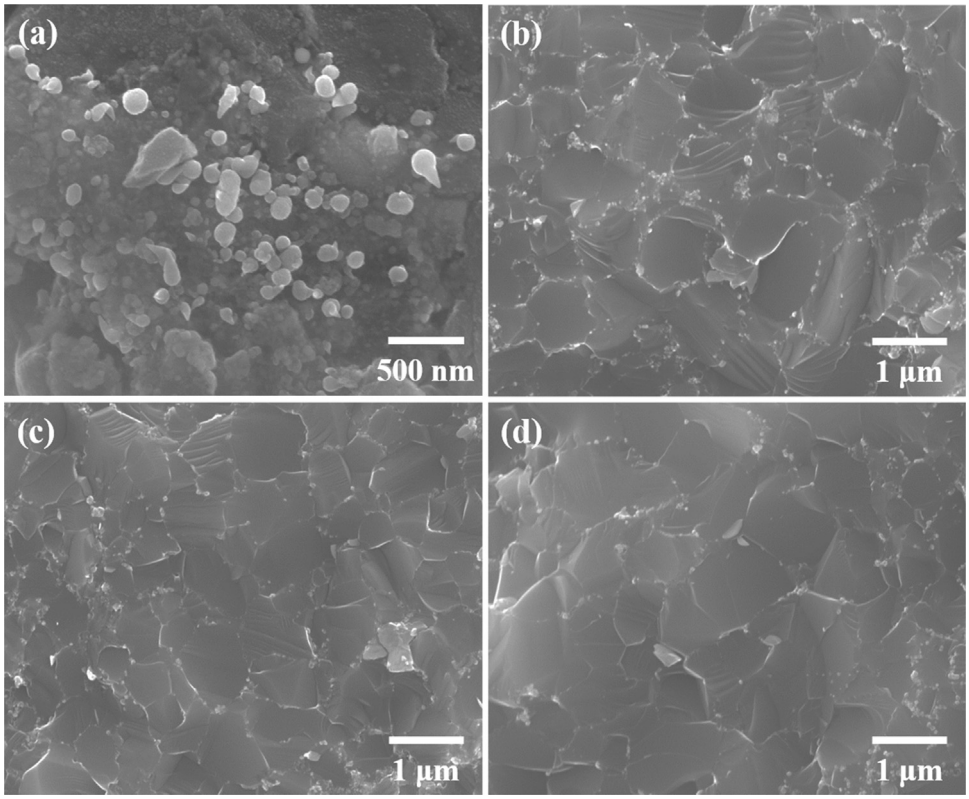

Fig. 1. SEM images of (a) hybrid powders decorated 0.6 vol% Cu particles and the fractured surface of 0.6 vol% (b) Cu, (c) Al, and (d) Sn decorated $Mg_{1.96}Al_{0.04}Si_{0.97}Bi_{0.03}$ samples.

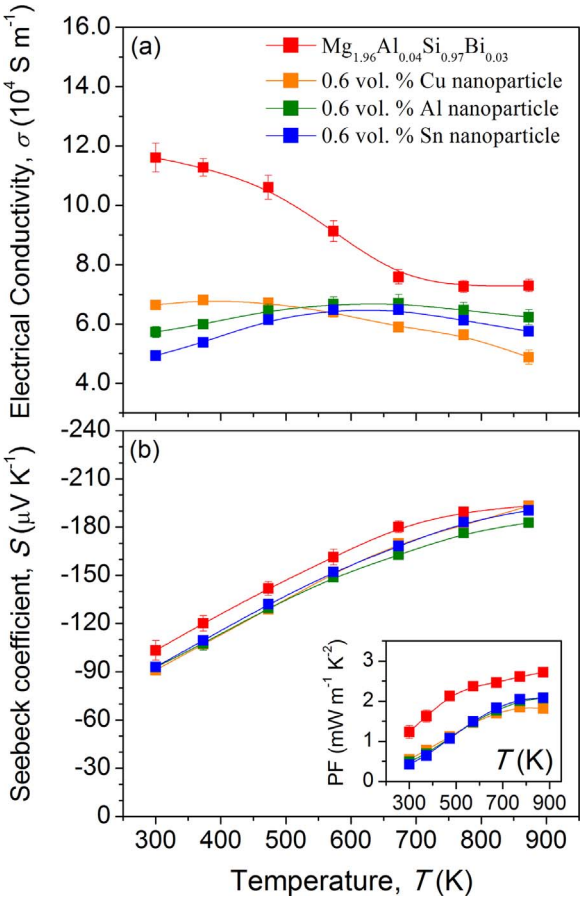

Fig. 2. Temperature dependence of (a) electrical conductivity, and (b) Seebeck coefficient for metal decorated $Mg_{1.96}Al_{0.04}Si_{0.97}Bi_{0.03}$ samples. The inset of (b) shows the power factor.

showed a size distribution partially due to the aggregation of metal nanoparticles during sintering. It was noted that the average grain size of the nanocomposites was ~1 μm smaller than that of the pristine sample (~3 μm) [1]. This was attributed to grain growth inhibition in the presence of insoluble metal nanoparticles at the grain boundaries, as shown in Fig. 1(b)–(d).

Fig. 2 shows the temperature dependence of the electronic transport properties for pristine $Mg_{1.96}Al_{0.04}Si_{0.97}Bi_{0.03}$ and 0.6 vol% Cu-, Al-, and Sn-nanoparticle-embedded nanocomposites. The σ values of all nanocomposites were lower than that of the pristine sample in the entire temperature range considered. To clarify this, we calculated n_c and μ_{Hall} by estimating a one-band model and listed them in Table 1. The n_c values for all samples were similar (8.96×10^{19}–9.61×10^{19} cm^{-3}), indicating that the reduction of σ on introduction of nanosized Cu, Al, and Sn originates from a decrease in the μ_{Hall} value.

Table 1
Room temperature electronic transport parameters for metal decorated $Mg_{1.96}Al_{0.04}Si_{0.97}Bi_{0.03}$ samples.

	σ (S m^{-1})	S (μV K^{-1})	n_c (cm^{-3})	μ_{Hall} (cm^2 V^{-1} s^{-1})
$Mg_{1.96}Al_{0.04}Si_{0.97}Bi_{0.03}$	122,596.24	−99.78	9.27×10^{19}	81.4
$Mg_{1.96}Al_{0.04}Si_{0.97}Bi_{0.03}$ + Cu 0.6 vol%	66,430.93	−91.06	9.61×10^{19}	42.5
$Mg_{1.96}Al_{0.04}Si_{0.97}Bi_{0.03}$ + Al 0.6 vol%	57,326.07	−92.77	8.96×10^{19}	39.3
$Mg_{1.96}Al_{0.04}Si_{0.97}Bi_{0.03}$ + Sn 0.6 vol%	49,329.00	−93.01	9.52×10^{19}	31.9

Thus, lower σ values of the nanocomposites are due to the deteriorated μ_{Hall} values (31.9–42.5 cm^2 V^{-1} s^{-1}) compared to that of the pristine sample (81.4 cm^2 V^{-1} s^{-1}) owing to intensified carrier scattering at the interface between $Mg_{1.96}Al_{0.04}Si_{0.97}Bi_{0.03}$ and metal nanoparticles. On the other hand, the values of S for all samples were very similar, suggesting that the value of S was not significantly affected in the presence of Cu, Al, and Sn nanoparticles. The slight decrease in the absolute values of S for nanocomposites was considered to be related with the low S values (6.5 μV K^{-1} for Cu, 3.5 μV K^{-1} for Al, and −1.5 μV K^{-1} for Sn) [16] of metal nanoparticles. This result is also explained by the density of states (DOS) effective mass (m_d^*) values estimated using the following equation [17]:

$$S = \frac{8\pi^2 k_B^2}{3eh^2}\left(\frac{\pi}{3n_c}\right)^{2/3} m^* T,$$

where k_B, e, and h are the Boltzmann constant, elementary charge, and Planck constant, respectively. The obtained values of m_d^* were almost the same (0.95 m_0) for all samples. Consequently, the power factor (σS^2) values of the nanocomposites (1.82–2.09 mW m^{-1} K^{-2} at 873 K) were lower than that of the pristine sample (2.72 mW m^{-1} K^{-2} at 873 K).

Fig. 3(a) shows the κ_{tot} for pristine $Mg_{1.96}Al_{0.04}Si_{0.97}Bi_{0.03}$ and 0.6 vol% Cu-, Al-, and Sn-nanoparticle-embedded nanocomposites. The κ_{tot} values of the nanocomposites (4.13–4.91 W m^{-1} K^{-1} at 373 K) were lower than that of the pristine sample (5.06 W m^{-1} K^{-1} at 373 K) and the lower κ_{tot} values of the nanocomposites were maintained throughout the temperature range considered. We calculated the lattice thermal conductivity κ_{lat} to elucidate the phonon scattering effect caused by the metal nanoinclusions (inset of Fig. 3(b)). The κ_{lat} values were estimated by subtracting the electronic contribu-

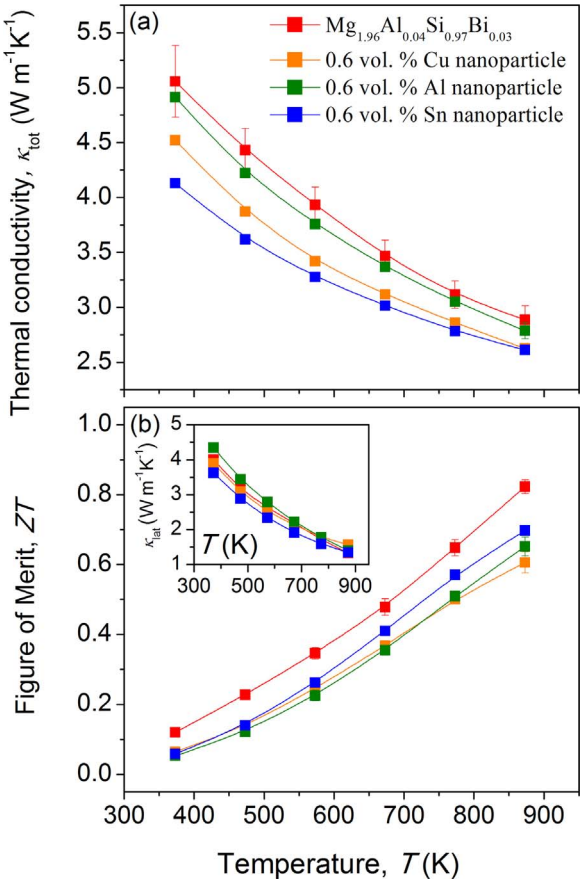

Fig. 3. Temperature dependence of (a) total thermal conductivity, and (b) ZT for metal decorated $Mg_{1.96}Al_{0.04}Si_{0.97}Bi_{0.03}$ samples. The inset of (b) shows lattice thermal conductivity.

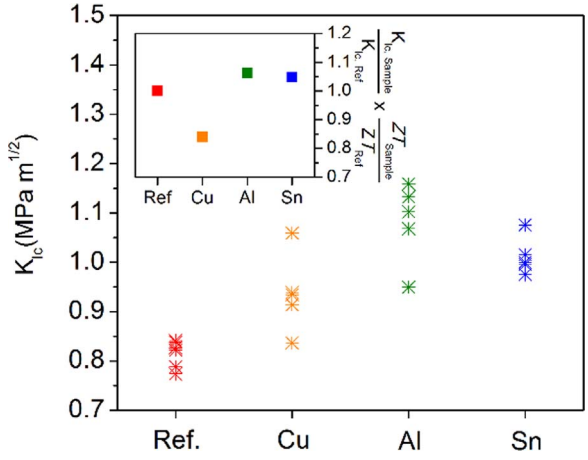

Fig. 4. Fracture toughness of Cu, Al, and Sn 0.6 vol% decorated $Mg_{1.96}Al_{0.04}Si_{0.97}Bi_{0.03}$ samples. The inset shows the quantitative comparison of nanocomposites.

tion κ_{ele} (= $L\sigma T$, where L is the Lorenz number) from κ_{tot}. The L was calculated using the following equation [18]:

$$L = \left(\frac{k_B}{e}\right)^2 \left(\frac{(r+7/2)F_{r+5/2}(\eta)}{(r+3/2)F_{r+1/2}(\eta)} - \left[\frac{(r+5/2)F_{r+3/2}(\eta)}{(r+3/2)F_{r+1/2}(\eta)}\right]^2 \right),$$

where η is the Fermi energy, $F_n(\eta)$ is the n-th order Fermi integral, and r is the scattering parameter, respectively. The κ_{lat} values for the samples did not exhibit significant differences, suggesting an off-set effect of the intensified phonon scattering at the interface between $Mg_{1.96}Al_{0.04}Si_{0.97}Bi_{0.03}$ and the metal nanoparticles and increased thermal conduction owing to the higher κ of metal nanoinclusions (401 W m^{-1} K^{-1} for Cu, 205 W m^{-1} K^{-1} for Al, and 67 W m^{-1} K^{-1} for Sn).

ZT values calculated from the measured σ, S, and κ_{tot} values are shown in Fig. 3(b). The ZT values of nanocomposites (0.61–0.70 at 873 K) were lower than that of the pristine sample (0.82 at 873 K) mainly due to the decreased power factor. Meanwhile, the fracture toughness of the nanocomposites improved compared to that of the pristine sample because of the high-fracture-toughness metal nanoparticles uniformly distributed at grain boundaries, as shown in Fig. 4. The fracture toughness was significantly enhanced by ~35% in 0.6 vol% Al-nanoparticle-embedded nanocomposites, indicating that the introduction of metal nanoinclusions with high mechanical properties (14–28 MPa m$^{1/2}$) could be an effective route toward enhanced mechanical reliability of TE materials because the nanoinclusions can interfere with crack propagation. To confirm the effect of each nanoparticle, we calculated $\frac{K_{Ic,Sample}}{K_{Ic,Ref}} \times \frac{ZT_{Sample}}{ZT_{Ref}}$ as shown in the inset of Fig. 4. Although the Sn-nanoparticle-embedded nanocomposites were effective in minimizing deterioration of thermoelectric properties, the introduction of Al nanoparticles was more effective in ensuring mechanical reliability. Control of the size and dispersibility of metal nanoinclusions to minimize carrier scattering and maximize toughening would be a critical factor in realizing simultaneous enhancement of TE and mechanical properties.

4. Conclusions

We fabricated nanocomposites of $Mg_{1.96}Al_{0.04}Si_{0.97}Bi_{0.03}$ with metal nanoparticles (Cu, Al, and Sn) uniformly embedded at grain boundaries by combining nanometal decoration and spark plasma sintering and evaluated their thermoelectric and mechanical properties. On the introduction of small amounts (~0.6 vol%) of Al nanoparticles (~150 nm), the fracture toughness was significantly enhanced by ~35% compared to that of pristine $Mg_{1.96}Al_{0.04}Si_{0.97}Bi_{0.03}$. However, the nanocomposites showed a trade-off between the fracture toughness and thermoelectric properties mainly owing to deteriorated electronic transport. This drawback could be improved by precise control of the chemical and physical characteristics of nanoparticles.

Acknowledgements

This work was supported by the Hyundai Motor Company (2016-11-0532), the National Research Foundation of Korea (NRF) Grant funded by the Korea government (MSIP) (2014R1A2A1A10053869), the Priority Research Centers Program (2009-0093823), and the Industrial Fundamental Technology Development Program (10052977) funded by the Ministry of Trade, Industry and Energy (MOTIE) of Korea.

References

[1] G. Kim, J. Kim, H. Lee, S. Cho, I. Lyo, S. Noh, B.W. Kim, S.W. Kim, K.H. Lee, W. Lee, Co-doping of Al and Bi to control the transport properties for improving thermoelectric performance of Mg_2Si, Scr. Mater. 116 (2016) 11–15.
[2] G. Kim, H. Lee, J. Kim, J.W. Roh, I. Lyo, B.W. Kim, K.H. Lee, W. Lee, Up-scaled solid state reaction for synthesis of doped Mg_2Si, Scr. Mater. 128 (2017) 53–56.
[3] M.E. Launey, R.O. Ritchie, On the fracture toughness of advanced materials, Adv. Mater. 21 (2009) 2103–2110.
[4] R.D. Schmidt, X. Fan, E.D. Case, P.B. Sarac, Mechanical properties of Mg_2Si thermoelectric materials with the addition of 0–4 vol% silicon carbide nanoparticles (SiCNP), J. Mater. Sci. 50 (2015) 4034–4046.
[5] L. Cheng, Z. Xie, G. Liu, W. Liu, W. Xue, Densification and mechanical properties of TiC by SPS-effects of holding time, sintering temperature and pressure condition, J. Eur. Ceram. Soc. 32 (2012) 3399–3406.
[6] D. Cai, Z. Yang, X. Duan, Q. Zhang, Q. Li, Q. Li, Y. Sun, D. Jia, Y. Zhou, Influence of sintering pressure on the crystallization and mechanical properties of BN-MAS composite ceramics, J. Mater. Sci. 51 (2016) 2292–2298.
[7] N. Claussen, Fracture toughness of Al_2O_3 with an unstabilized ZrO_2 dispersed phase, J. Am. Ceram. Soc. 59 (1976) 49–51.
[8] W. Naous, X.Y. Yu, Q.X. Zhang, K. Naito, Y. Kagawa, Morphology, tensile properties, and fracture toughness of epoxy/Al_2O_3 nanocomposites, J. Polym. Sci. Polym. Phys. 44 (2006) 1466–1473.
[9] K. Yin, X. Su, Y. Yan, H. Tang, M.G. Kanatzidis, C. Uher, X. Tang, Morphology modulation of SiC nano-additives for mechanical robust high thermoelectric performance $Mg_2Si_{1-x}Sn_x$/SiC nano-composites, Scr. Mater. 126 (2017) 1–5.
[10] G.D. Zhan, H.D. Kuntz, J. Wan, A.K. Mukherjee, Single-wall carbon nanotubes as attractive toughening agents in alumina-based nanocomposites, Nat. Mater. 2 (2003) 38–42.
[11] L.S. Walker, V.R. Marotto, M.A. Rafiee, N. Koratkar, E.L. Corral, Toughening in graphene ceramic composites, ACS Nano 5 (2011) 3182–3190.
[12] S. Hwang, S.I. Kim, K. Ahn, J.W. Roh, D.J. Yang, S.M. Lee, K.H. Lee, Enhancing the thermoelectric properties of p-type bulk Bi-Sb-Te nanocomposites via solution-based metal nanoparticle decoration, J. Electron. Mater. 42 (2013) 1411–1416.
[13] K.H. Lee, H.S. Kim, S.I. Kim, E.S. Lee, S.M. Lee, J.S. Rhyee, J.Y. Jung, I.H. Kim, Y. Wang, K. Koumoto, Enhancement of thermoelectric figure of merit for $Bi_{0.5}Sb_{1.5}Te_3$ by metal nanoparticle decoration, J. Electron. Mater. 41 (2012) 1165–1169.
[14] Y. Lin, K.A. Watson, M.J. Fallbach, S. Ghose, J.G. Smith, Jr.D.M. Delozier, W. Cao, R.E. Crooks, J.W. Connell, Rapid, solventless, bulk preparation of metal nanoparticle-decorated carbon nanotubes, ACS Nano 3 (2009) 871–884.
[15] J.J. Kruzic, R.O. Ritchie, Determining the toughness of ceramics from vickers indentations using the crack-opening displacements: an experimental study, J. Am. Ceram. Soc. 86 (2003) 1433–1436.
[16] P. Fiflis, L. Kirsch, D. Andruczyk, D. Curreli, D.N. Ruzic, Seebeck coefficient measurements on Li, Sn, Ta, Mo, and W, J. Nucl. Mater. 438 (2013) 224–227.
[17] G.J. Snyder, E.S. Toberer, Complex thermoelectric materials, Nat. Mater. 7 (2008) 105–114.
[18] L.D. Zhao, S.H. Lo, J.Q. He, H. Li, K. Biswas, J. Androulakis, C.I. Wu, T.P. Hogan, D.Y. Chung, V.P. Dravid, M.G. Kanatzidis, High performance thermoelectrics from earth-abundant materials: enhanced figure of merit in PbS by second phase nanostructures, J. Am. Chem. Soc. 133 (2011) 20476–20487.